Theoretical and Applied Fracture Mechanics 121 (2022) 103527

Contents lists available at ScienceDirect

Theoretical and Applied Fracture Mechanics

journal homepage: www.elsevier.com/locate/tafmec

Mixed-mode I/II fracture properties of selectively laser sintered polyamide

Dan Ioan Stoia, Emanoil Linul *, Liviu Marsavina

Department of Mechanics and Strength of Materials, Politehnica University Timisoara, Blvd. M. Viteazu No. 1, 300 222 Timisoara, Romania

ARTICLE INFO

Keywords:
mixed-mode I/II fracture
Laser-sintered polyamide
Fracture toughness
Crack paths
Fracture criteria

ABSTRACT

Additive manufacturing (AM) is a topical field today and has received the attention of many researchers. However, further research is needed to overcome the many challenges facing AM, especially in the mixed-mode fracture. The results presented in this paper are framing the experimental data obtained for mixed-mode I/II fracture properties of laser sintered polyamide. The experiment was carried out on Semi-Circular Bend (SCB) specimens manufactured from polyamide PA2200 using EOS Formiga P100 laser sintering machine. To achieve the full range of fracture toughness values, from pure mode I to pure mode II, five crack orientations of the SCB specimens (0, 15, 30, 45 and 54°) were considered. Further, crack initiation angle and crack paths of SCB specimens have been assessed in order to identify the fracture phenomena (interlayer and/or intralayer fracture). The main fracture properties (fracture toughness, crack initiation angles and crack paths) were compared with the theoretical predictions of three mixed-mode fracture criteria (Maximum Tensile Stress-MTS, Maximum Energy Release Rate-Gmax and Equivalent Stress Intensity Factor-ESIF). The results underline differences between theoretical approaches and experimental data, especially due to the interlayer fracture phenomenon. However, it was obtained that the Gmax and ESIF criteria show the best match with the experimental data.

1. Introduction

Additive manufacturing (AM) or additive layer manufacturing (ALM) is characterized by a set of manufacturing processes, capable of producing complex three-dimensional (3D) objects directly from a Computer-aided design (CAD) model [1–3]. Research and approaches in the field of 3D printing are intensely developed, however, one of the challenges of AM components is to obtain consistent properties by using the same material [4–6]. Today there is no standardization of the manufacturing parameters and testing procedures, because the influence of technological parameters upon mechanical and fracture properties is not clear so far [7,8]. Especially in Selective Laser Sintering (SLS), phenomena like electrostatic charge of the particles, the interaction between laser and powder bed, the powder purity, are highly influencing the components at the structural level, and therefore all the mechanical and physical properties [9–11].

In real-life applications, engineering structures are not only subjected to tensile but also experience torsion and shear loading, which implicitly induce a mixed-mode fracture (e.g. I/II, I/III, II/III, I/II/III). In general, the mixed-mode phenomenon is quite complex, especially for layer-by-layer 3D printed components. A significant number of experimental methods and various specimen configurations have been developed and employed to measure the mixed-mode fracture properties (fracture toughness, crack growth mechanisms, etc.) of different engineering materials. In this regard, specimens geometries such as brazilian disk (BD) [12–14], short beam bending (SBB) [15–20], asymmetric short bend beam specimen (ASBB) [21], asymmetric semi-circular bend (ASCB) [16,22–25], edge cracked triangular-ECT [14,26,27], diagonally loaded square plate (DLSP) [13,28], edge notched disc bend (ENDB) [14,23,29], asymmetric edge notch disc bend (AENDB) [60], inclined edge crack asymmetric bend (IE-CAB) [30], asymmetric four-point bend (AFPB) [13,14,25,31], compact tension-shear (CTS) [14,23] and others have been used over time to assess the mixed-mode fracture behavior of advanced materials. However, one of the most popular tests for determining the mixed-mode I/II fracture behavior of brittle materials is obtained by using the semi-circular bend (SCB) specimen [13,26]. The popularity of this specimen comes from its ability to vary the loading mode, from pure mode I to pure mode II, by simply changing the crack angle relative to the loading direction. Unlike the case of traditional materials, the insertion of a crack in the AM specimens is very simple, this being obtained from the printing stage.

There are consistent studies on mixed-mode fracture mechanics determined on SCB specimens of various homogenous brittle materials [32–34]. Ayatollahi et.al. [32] present the mixed mode fracture of

* Corresponding author.
E-mail address: emanoil.linul@upt.ro (E. Linul).

https://doi.org/10.1016/j.tafmec.2022.103527
Received 21 March 2022; Received in revised form 1 July 2022; Accepted 1 August 2022
Available online 4 August 2022

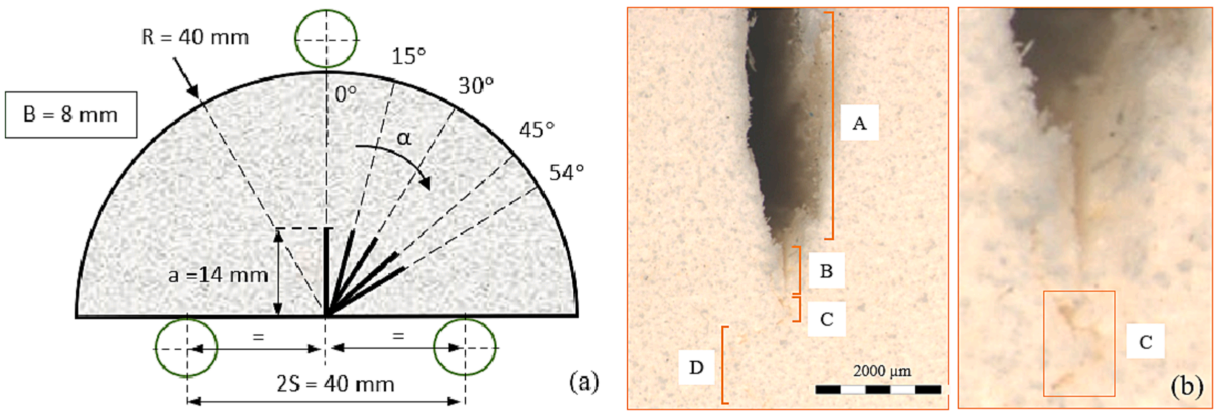

Fig. 1. SCB specimen design and loading mode (a) and crack at 0° (b): A-partial view of pre-crack length; B-sharpened crack tip; C-initiation angle; D-crack path.

PMMA in the full range from pure mode I to pure mode II. The study was conducted on cracked SCB in order to determine the fracture load and crack path. They employed a modified theoretical MTS criterion that give a much better estimation with the experimental results. Aliha et.al. [33] used marble rock SCB specimens for investigating the mixed mode I/II fracture toughness. Also, in this case was found that an improved fracture criterion (Generalized Maximum Tangential Stress) can provide better estimation of the experiments. Marsavina et.al. [34] conducted investigations using Asymmetric Semi-Circular Bend (ASCB) specimens on three types of PUR foams. The experimental results reveal the fracture toughness of these foams in relation to the density, cell orientation, loading speed and mixed mode loading.

Some other studies approach the mixed-mode fracture properties of additively manufactured materials. Ameri et al [35] used five different materials processed by FDM in order to underline the possibilities to decrease the amount of anisotropy and void volume, and the influence of those on mixed-mode fracture behavior. The SCB specimens were subjected to symmetrical three-point bending test and the fracture load and crack initiation angles were associated with the presence of open holes inside the specimens. The effect of printing orientation on the mixed-mode I/II fracture behavior of polycarbonate SCB specimens manufactured by FDM was approached by Bahrami et.al [36]. The fracture toughness results according to the layer directions were extracted from fracture load data and compared to the theoretical fracture criterion MTS and GMTS. Again, the GMTS criterion gives a better prediction for additive samples.

Large efforts concerning fracture toughness of AM polymers are relying on Fused Deposition Modeling (FDM) due to the accessibility of FDM both in machine and primary material costs and also in technology [37–39]. The influence of layer orientation respecting to the loading direction, the infill speed and density, the used polymer, the layer thickness and the raster angle are all process parameters that had being considered as variables in order to determine the outcome mechanical properties [40–42,43]. Consistently, the results show orthotropic mechanical properties according to the direction of manufacturing layers. Recent research reveals the dynamic behavior of FDM manufactured samples by providing the fracture energies in pure mode I and II which are several times higher than in static state [44].

Fracture properties of laser-sintered polyamide were approached by some authors considering a strong elastic–plastic behavior of it and therefore using the J-integral as characterization parameter. Experiments based on inclined edge cracked semi-circular specimen subjected to asymmetric three-point bend loading (IASCB), digital image correlation (DIC) of full-field displacement and numerical simulations, were used to determine the geometrical factors and to compute the J-integral. The J-integral of mixed-mode I/II give comparable results for both methods and demonstrate its variation with mode mixity ratio [45]. The IASCB specimens were successfully used in mixed-mode fracture toughness characterization of SLS metal parts. The stress intensity factors were computed based on DIC fitting and compared to the ones obtained by conventional critical load method. The data from both methods show a good fit based on local stress criterion, as was proposed by Yongming Liu [46,47].

Studying the literature, it was found that the SCB specimen was used mostly in the case of components printed by FDM technology. There are no papers that report the mixed mode I/II fracture properties for SCB specimens manufactured by the SLS process. In our previous study, the authors present the influence of energy density on mode I and II fracture toughness of laser sintered polyamide, revealing a direct tendency of property growing with energy input [48]. The purpose of the investigation is to determine the fracture properties of laser sintered polyamide PA2200, according to the crack orientations of 0, 15, 30, 45 and 54°. The properties include mixed mode I/II stress intensity factors both as experimental results and predictions according to fracture criteria. Also, measured and predicted crack initiation angles and crack path were presented in order to identify the effect of layer manufacturing on fracture behavior. The novelty of the research is approaching the fracture mechanics of laser sintered specimens rather than FDM. In SLS, different variables are directly influencing the fracture behavior of the samples: temperatures, energy density, quasi-uniform distribution of powder particles, electrostatic charge of the powder, powder humidity, sample orientation, laser optics and others. For all of these reasons, the results obtained for different additive manufacturing technologies are not (or only partial) applying to SLS.

2. Materials and methods

2.1. Specimen design, material and fabrication

The material used was polyamide PA2200 commercially available from Electro Optical Systems - EOS GmbH, Krailling, Germany. The interest in characterizing this polymer is the wide range of its use in technical applications like automotive industry and medical field. Also, the large sinterization window make it a good candidate for powder bed fusion.

To extract the fracture properties of Selective Laser Sintered (SLS) printed parts, Semi-Circular Bend (SCB) specimen was used. Fig. 1a shows the geometric parameters of the specimen. The SCB design was conducted in SolidWorks2020 (3DS North American HQ, USA) considering the following dimensions: the radius R = 40 mm, the thickness B = 8 mm, the span length 2S = 40 mm and the initial crack length a = 14 mm. For considering the effect of mode mixity, the directions of the cracks were designed at five individual angles: 0, 15, 30, 45 and 54°, measured relative to the vertical line of loading. Thus, the crack at 0° represents a fracture in pure mode I, while a crack inclined at 54° defines the pure mode II of fracture. Between the two extreme angles (0

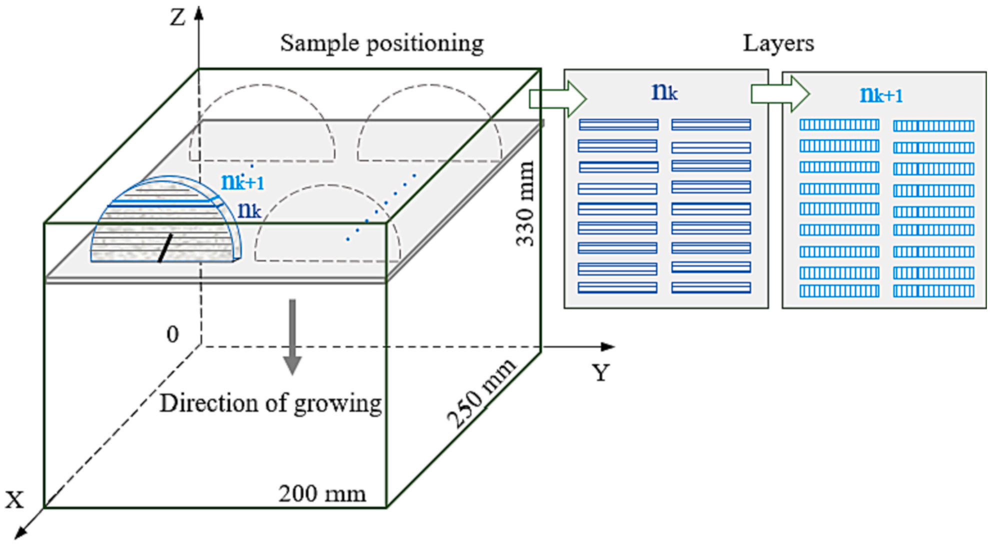

Fig. 2. Distribution of SCB specimens on the Formiga P100 platform and hatching directions.

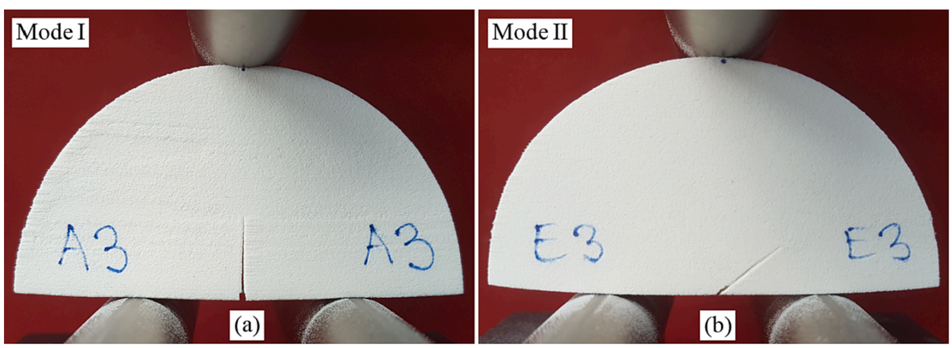

Fig. 3. Test setup for mode I (a) and mode II (b) fracture.

and 54°), there are three mixed modes I/II of fracture (15, 30 and 45°).

The cracks were designed in CAD and directly manufactured through SLS process. Before testing, the crack tip of each specimen was sharpened manually, using a cutter blade. We take attention that the pressure exerted on the blade to be relatively constant, so the sharp edge of the crack tip has a constant penetration. A microscopic image obtained after testing can be observed in the Fig. 1b, were the domains of pre-crack length, sharpened crack tip, fracture initiation angle and crack path can be identified.

In order to obtain the repeatability of results, five specimens were manufactured for each crack angle. All 25 specimens were manufactured by laser sintering under the same conditions, using the EOS Formiga P100 (Electro Optical Systems - EOS GmbH, Krailling, Germany) machine. The orientation of the part was chosen to obtain the manufactured layers perpendicular to the loading direction, in order to avoid delamination [49]. To improve the interlayer bonding, sintering was

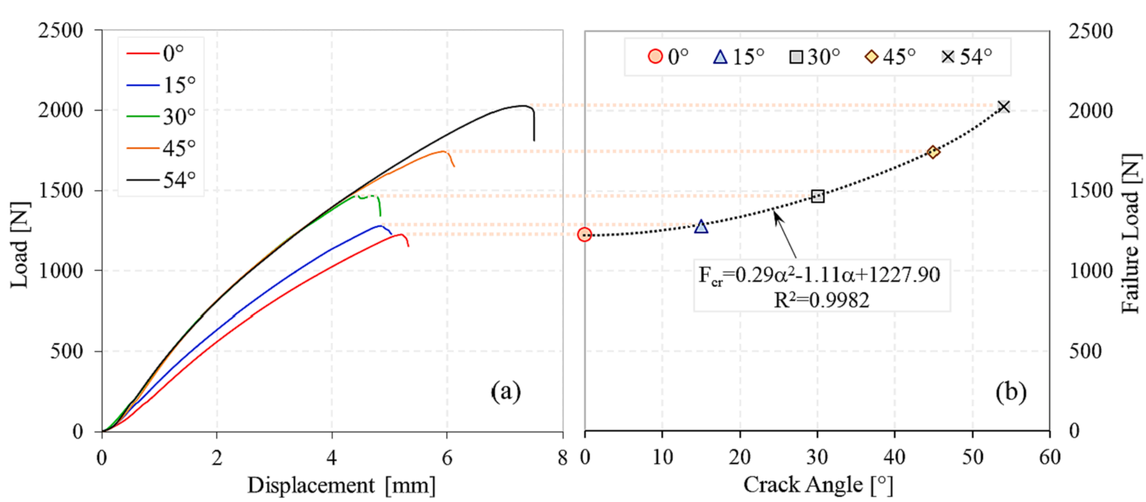

Fig. 4. Load-displacement curves of SCB specimens under 3 PB test with different crack angles (a) and the variation of the failure load with the crack angle (b).

Table 1
Fracture loads for the SLS-PA2200 printed specimens.

Sample code	Crack angle [°]	Fracture load [N]	Average load [N]	Standard deviation [N]
A1	0	1240	1365.01	310.9
A2	0	1860		
A3	0	1050		
A4	0	1450		
A5	0	1225		
B1	15	1610	1293.8	288.0
B2	15	1340		
B3	15	1280		
B4	15	829		
B5	15	1410		
C1	30	1470	1244.0	150.4
C2	30	1280		
C3	30	1180		
C4	30	1230		
C5	30	1060		
D1	45	2170	1876.0	376.3
D2	45	2370		
D3	45	1600		
D4	45	1740		
D5	45	1500		
E1	54	2026	1866.2	143.7
E2	54	1998		
E3	54	1845		
E4	54	1768		
E5	54	1694		

performed in a cross-hatching manner (Fig. 2) by alternating the X and Y scanning directions.

The process was conducted considering the following parameters: energy density 0.066 J/mm^2, beam offset 0.15 mm, process chamber temperature 170 °C, removal chamber temperature 152 °C, layer thickness 0.1 mm and a uniform scaling factor of 2 %.

2.2. Mechanical testing

The experimental investigations were carried out on a 5 kN Zwick-Roell universal testing machine, using a 3-point bending (3 PB) fixture. The span of lower support pins was set to 40 mm, while the upper loading pin was placed symmetrical between support pins. Fig. 3 shows the SCB specimen placed on the 3 PB device for both mode I (Fig. 3a) and mode II (Fig. 3b) loading. The loading and support pins had a diameter of 20 mm, in order to minimize the effect of indentation, experimentally determined by the authors in earlier studies. However, indentation on this material will always occur at some extent, due to its porous structure that led to localized stiffness degradation.

All tests were conducted at a loading velocity of 5 mm/min and a sampling rate of 600 Hz. The experiments were performed at room temperature, according to the ASTM D5045-14 standard [50].

2.3. Crack measurements

Crack initiation angles and crack paths were determined for each individual specimen on digital 40 mega pixels images of the front SCB view. The image digitization and processing were done in ImageJ (Image processing and analysis in Java) free software. The image calibration was set based on a ruler of 500 μm resolution.

3. Results and discussions

3.1. Fracture toughness

The current section presents the main results of the fracture tests. At the end of each test, the load–displacement data were subsequently exported for further processing. The SCB specimens were loaded under a 3 PB condition to the breaking point. Fig. 4a presents the load–displacement curves of SLS printed parts for various crack angles (0, 15, 30, 45 and 54°), while Fig. 4b depict the variation of the failure loads of the SCB specimens with the crack angles under 3 PB tests. Regardless of the value of the crack angle, the load–displacement curves show a quasi-brittle behavior [51,52]. The failure behavior of fractured SCB specimens satisfies the linear elastic fracture mechanics (LEFM) conditions (the small scale yielding condition). In the case of the present study, the plastic zone is restricted to a sufficiently small extension in relation to the dimensions of the crack. Therefore, the nonlinear zone ahead of the crack tip is small compared to the characteristic dimensions of the specimen. The slightly nonlinear pattern prior to the fracture point is associated with the indentation of the 3D-printed SCB specimens in the area of the support and loading pins (detailed discussions are associated with Fig. 7). Moreover, according to the ASTM D5045-14 standard [50], the 5 % slope of each individual curve included maximum load.

Table 2
Values of Y_I and Y_{II} non-dimensional stress intensity factors.

Crack angle α	**0°**	**15°**	**30°**	**45°**	**54°**
Me [°]	1.000	4.286	0.624	0.342	0.000
Y_I [-]	2.787	2.399	1.461	0.518	0.000
Y_{II} [-]	0.000	0.834	0.978	0.871	0.659

According to Fig. 4b, the failure load (F_{cr}) increases according to a second order polynomial with increasing crack angle, with a very good coefficient of determination of $R^2 = 0.9982$. The higher fracture loads and largest displacements are obtained for the pure mode II loading. This means that by increasing the crack angle, from 0 to 54°, the presence of shear mode loading (i.e., mode II fracture) results in higher strength. Table 1 presents the details of fracture loads for all tested SCB printed specimens. Also given in this table are the mean values and standard deviations corresponding to each crack angle.

The pure mode I (K_I) and pure mode II (K_{II}) stress intensity factors (SIFs) values of each SCB specimen are calculated by based on numerical Eqs. (1) and (2) [32].

$$K_I = \sigma_{cr}\sqrt{\pi a}Y_I \tag{1}$$

$$K_{II} = \sigma_{cr}\sqrt{\pi a}Y_{II} \tag{2}$$

with.

$$\sigma_{cr} = \frac{F_{cr}}{2RB} \tag{3}$$

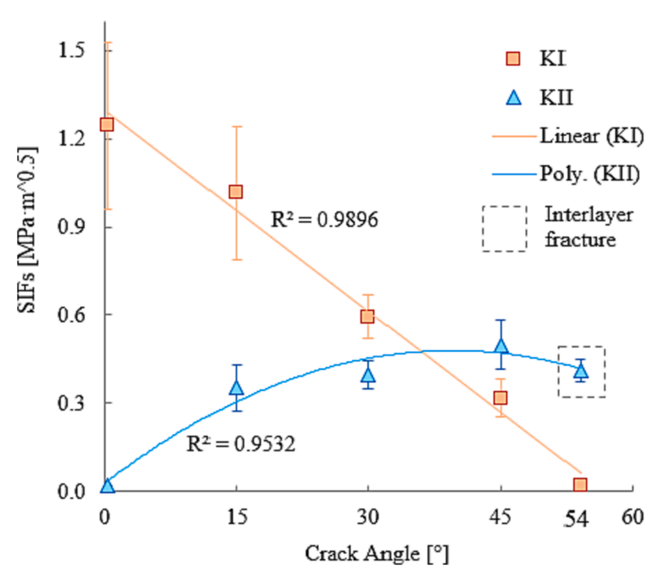

Fig. 5. SIFs variation in mixed-mode I/II fracture.

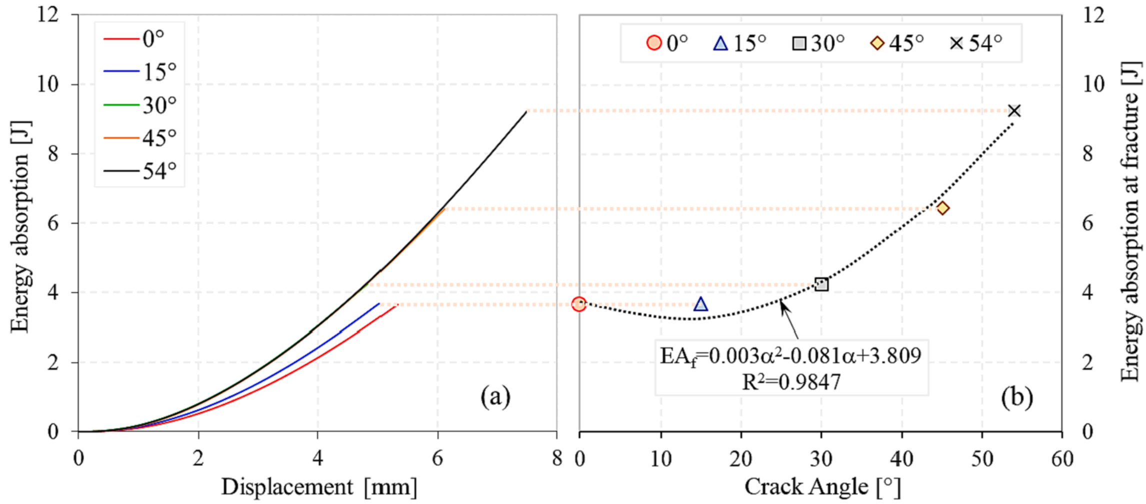

Fig. 6. Energy absorption-displacement curves (a) and the variation of the energy absorption at fracture with the crack angle (b).

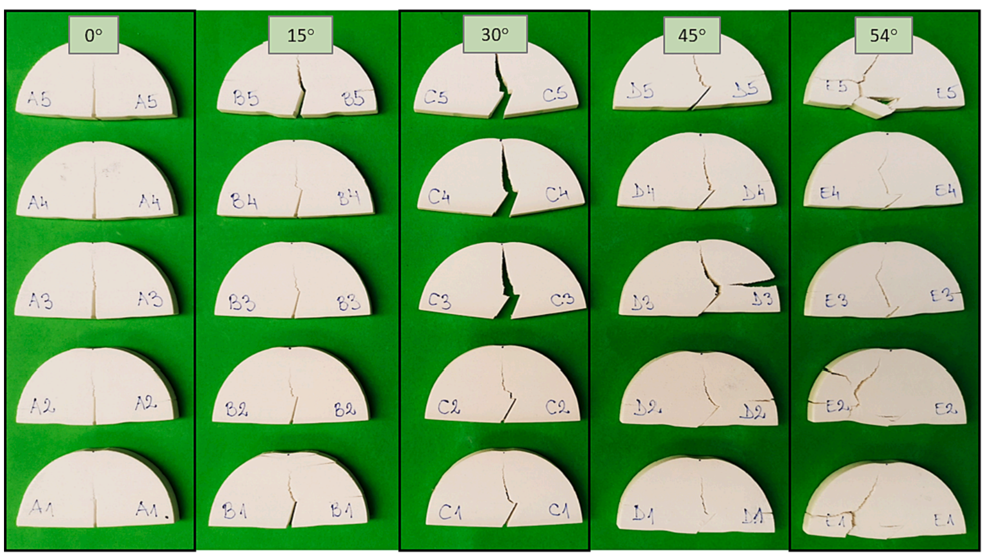

Fig. 7. Fractured SCB specimens for different crack angles.

where σ_{cr} is the uniform stress distribution in the SCB specimen without any discontinuity; F_{cr} is critical failure load of the SCB specimen in the pure modes I and II, respectively; Y_I and Y_{II} are the non-dimensional SIFs under pure modes I and II, respectively.

The values of the Y_I and Y_{II} non-dimensional SIFs, obtained from the finite element analysis (FEA) conducted in FRANC2D software are presented in Table 2 together with the mixing parameter $Me = arctg(K_{II}/K_I)$ [53]. The obtained results for Y_I and Y_{II} are in accordance with those presented in the literature by other researchers on SCB specimens [54,55]. The model was constructed by considering the Plain Stress settings and using the geometry shape and size identical to the experiment while the loading configuration of symmetric three-point bending was used to also replicate the experiments. All elastic properties required for FEA were experimentally determined in our previous work [56,57].

The results of SIFs determined with the equations (1) and (2) are graphically depicted in the Fig. 5, according to the crack angle. The K_I variation from 0° (pure mode 1) to 54° crack angle exhibits linear trend, with a coefficient of determination of $R^2 = 0.9896$, estimating a stress condition around the crack tip that for 0° will lead to rapid and unstable crack propagation. The trend of K_{II} according to crack angle can be approximated by a second order polynomial function of $R^2 = 0.9532$, exhibiting its maximum at 45° crack angle, while at 54° the interlayer fracture occurs. The results here presented are correlated with the trends obtained by Aliha for brittle SCB specimens in symmetrical three-point bending fracture tests [33].

On the other hand, high loads and implicitly high fracture toughness mean higher absorbed energy (EA). Therefore, the EA can be used as an appropriate measure to evaluate the crack growth initiation. Energy absorption-displacement curves of the 3D-printed SCB specimens under 3 PB test with different crack angles are shown in Fig. 6a.

The EA curves are presented up to the failure load F_{cr}, the onset of specimen fracture. The EA was calculated as the area under the load–displacement curve of the SCB specimen resulting from 3 PB test. Fig. 6b presents the variation of the energy absorption at fracture (EA_f) with the crack angle. The EA_f is varying as second order polynomial function with the crack angle. The fracture energy in mode II loading is about 60.5 % higher than the one in mode I.

Following 3 PB tests, the fractured SCB specimens were photographed both for determining the crack initiation angle and for identifying the crack growing direction. The direction of crack propagation according to crack angles is presented in Fig. 7. It has been found that

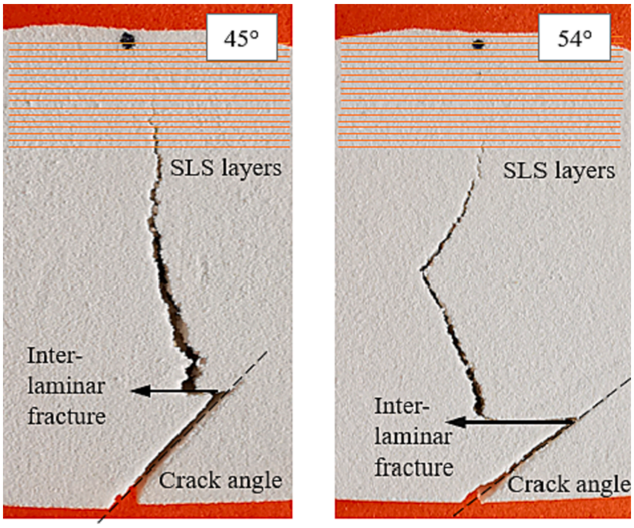

Fig. 8. Inter-laminar fracture observed for some 45° and 54° crack angles specimens.

during the experimental tests, some of the specimens experienced delamination, especially in dominant mode II (45°) and mode II (54°) loading. The practical ability of SCB specimen for fracture analyses of brittle materials such as PMMA, PU foams and rock has been demonstrated in previous woks [23–25,58–60]. Recently, some studies performed on 3D-printed SCB specimens using FDM technologies have strengthened the idea of using this geometry [35,36,43,44,61]. In the case of printed specimens (e.g. PLA, ABS, PA etc.), due to the layer-by-layer manufacturing process, small deviations, such as interlaminar fracture, from conventional materials (e.g. PMMA, rocks etc.) were observed. However, in the present study it was observed that delamination, because it occurs after the appearance of maximum load, influences to some extent only the crack path. Therefore, the other two properties represented by the crack initiation angle and the fracture toughness value are not affected by this isolated phenomenon.

In fracture mechanics studies conducted on FDM components [43,44] three major failure modes are described: fracture between layer (inter-laminar), fracture through layers (cross-laminar) and mixed cross/inter-laminar fracture. The results on FDM samples conclude that when cross laminar failure occur, the fracture toughness is increasing. Also, inter-laminar fracture along the printing direction was observed for pure mode I, while inter/cross laminar fracture occurred for the pure mode II. Our study reveals inter-laminar fracture when approaching pure mode II, for 45° and 54° samples (Fig. 8), and therefore the fracture energy in pure mode II was lower than expected.

Even if larger diameter pins were used, the SCB specimens show plastic deformations both in the area of the support pins and under the loading pin. This plastic indentation gradually increases with increasing load, especially where mode II loading is dominant. The size of the damaged area around the pins decreases with decreasing crack angle (from 54° to 0°), i.e. with the transition from pure mode II to mode I loading. The same phenomena (high plasticity in the pine area and delamination) was observed by Ameri et al [35] on PLA FDM printed parts.

Fig. 9 illustrates the measurements of crack initiation angle θ and the crack propagation points for the mixed-mode I/II fracture, for $\alpha = 30°$. Five angular measurements were conducted for each fractured sample, in order to compute an average initiation angle. The same procedure was followed for all five crack angles (0, 15, 30, 45 and 54°).

The average values of the θ angles for each crack angle are listed in Table 3, together with the corresponding standard deviations. Here the influence of two factors can be underlined: firstly, the differences in initiation angles among the five samples of the same crack angle and secondly the influence of the human consideration regarding the initiation direction. First factor is in close connection with the sintering homogeneity in the vicinity of the crack tip, while the second depends on image resolution. All in all, as data shows, the initiation angles are rather an angular interval than a unique value. The data also shows that in pure mode I fracture, the real initiation angle is never zero, as theory indicates.

Fig. 10 presents the experimental and numerical crack propagation paths in SCB specimens. The curvature differences between simulation data and real measured data are clearly noticeable. The FEA simulation obtained in our previous study [62] indicates a smooth transition, characterized by a large radius, from mixed-mode to pure mode I, and was presented here for observing the real crack path tendency. Regardless of the crack angle, the experimental fracture path trajectory is not smooth and straight (like for homogeneous materials with brittle or quasi-brittle behavior), but has a zig-zag pattern growth. In this case, the layered and orthotropic nature of the SLS parts dictates this trajectory. Generally, the crack is propagated along the weaker plane, following the alternating transition between *interlayer* fracture and *intralayer* fracture.

As shown in Fig. 10, the crack trajectories obtained from the experiments are consistent with those obtained from Franc2D simulations. Exceptions to this rule are the results obtained for pure mode II loading, which differ significantly.

Under 3 PB test, the layer-by-layer process of SLS shows its drawbacks. The part experiences a combination of interlayer and intralayer fracture, depending on the in-plane vs vertical particle sinterization. The intralayer fracture is identified in the case of the pure mode I loading or in mixed-mode I/II, but predominantly towards mode I. On the other hand, interlayer fracture or a combination of inter/intra layer fracture

Table 3
Average values of crack initiation angles, θ, in SCB specimens.

Crack angle, α [°]	0	15	30	45	54
Crack initiation angle, θ [°]	11.28 ± 2.46	32.96 ± 9.36	35.25 ± 5.03	55.39 ± 6.09	67.54 ± 4.25

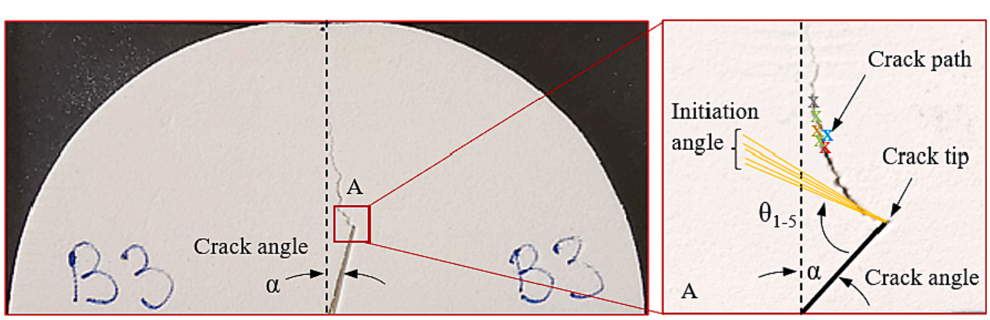

Fig. 9. The process of measuring crack initiation angles and crack paths in SCB specimens.

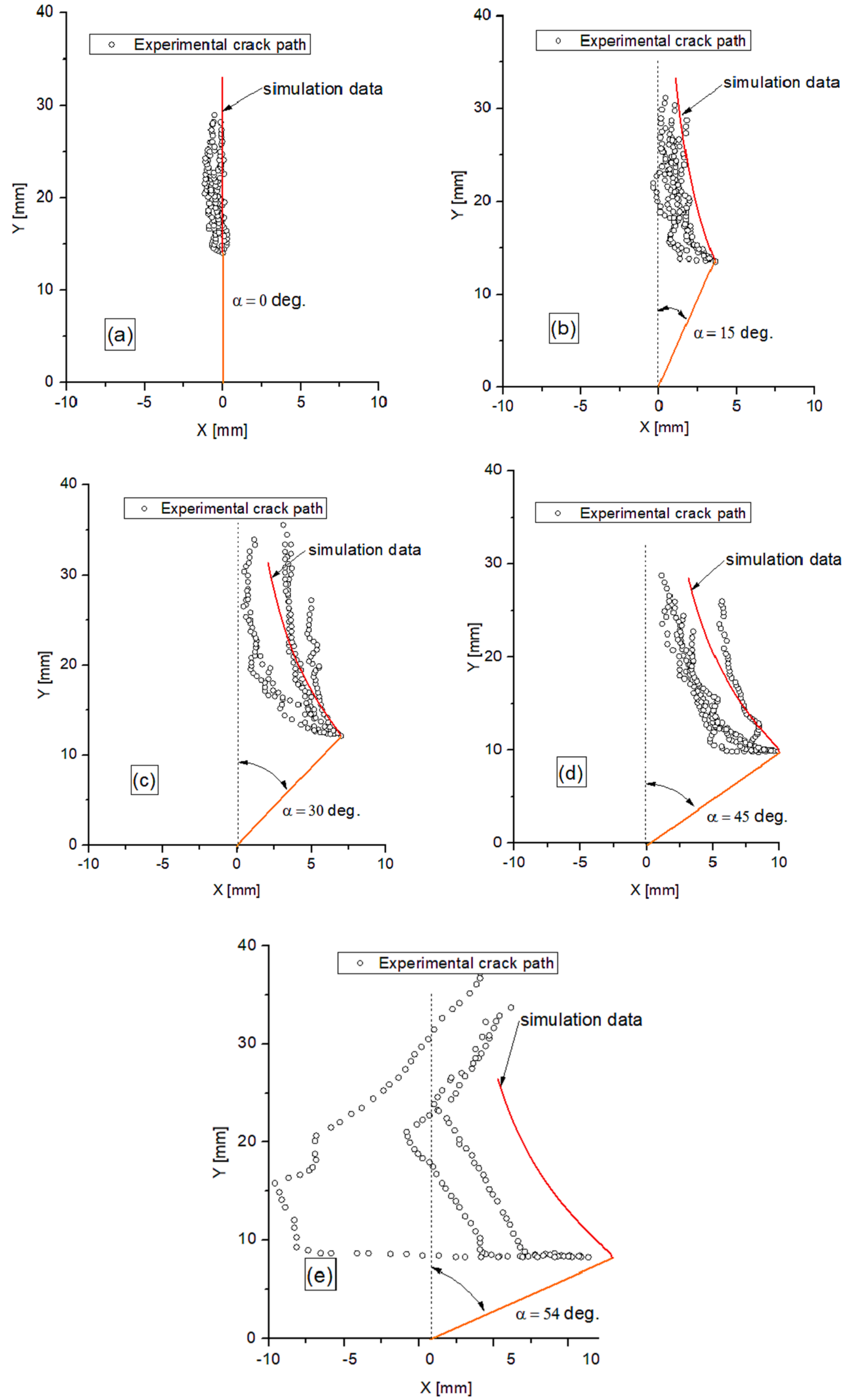

Fig. 10. Experimental and predicted crack growth path for the 3D-printed SCB specimens with 0 (a), 15 (b), 30 (c), 45 (d) and 54 (e) crack angle.

occurs in the pure mode II loading and mixed-mode I/II, but predominantly towards mode II. Specimen failure under in-plane shear (mode II) is always more complex than tensile opening fracture (mode I). In addition, mode II loading requires a higher load for the propagation of cracks in the tested specimens.

3.2. Mixed mode fracture criteria

In this section, fracture toughness and crack initiation angles are predicted employing different fracture criteria. For the general in-plane mixed mode case, a fracture criterion should provide both the crack initiation angle (θ_c) and a critical combination of SIFs (K_I and K_{II}) and fracture toughness (K_{IC}) in the $F(K_I, K_{II}, K_{IC}) = 0$ form. Over the years, several fracture criteria such as Maximum Tensile Stress (MTS), Generalized Maximum Tangential Stress (GMTS), Strain Energy Density (SED), Generalized Strain Energy Density (GSED), Maximum Tangential Strain (MTSN), Extended Maximum Tangential Strain (EMTSN), Equivalent Stress Intensity Factor (ESIF), Maximum Energy Release Rate (Gmax) and other have been developed and further improved/modified [59–61,63–65]. In the present study, the MTS, Gmax and ESIF criteria were considered suitable for describing fracture properties in laser sintered parts, and therefore used.

3.2.1. Maximum circumferential tensile stress (MTS) criterion

According to this criterion, the crack growth starts radially from the crack tip at an angle $\theta = \theta_c$ perpendicular to the maximum circumferential tensile stress [66]. The crack propagation became unstable when stress reaches a critical value, which is a material dependent parameter. The fracture toughness and prediction of crack initiation angle are computed according to Eqs. (4) and (5).

$$K_{IC} = cos\frac{\theta_c}{2}\left(K_I cos^2\frac{\theta_c}{2} - \frac{3}{2}K_{II} sin\theta_c\right) \tag{4}$$

$$\theta_c = -arccos\left(\frac{3K_{II}^2 + K_I\sqrt{K_I^2 + 8K_{II}^2}}{K_I^2 + 9K_{II}^2}\right) \tag{5}$$

3.2.2. Maximum energy release rate (Gmax) criterion

Maximum energy release rate criterion investigates the infinitesimal kink of a crack at an angle θ, and expressed the energy release rate in terms of stress intensity factors of initial crack [67]. The energy release rate and prediction of crack initiation angle are computed using Eqs. (6) and (7).

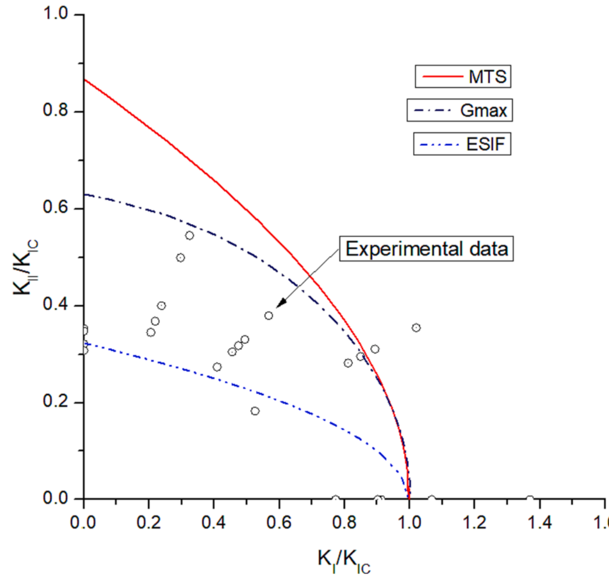

Fig. 11. Experimental results and theoretical predictions of mixed-mode I/II fracture toughness of SLS polyamide parts.

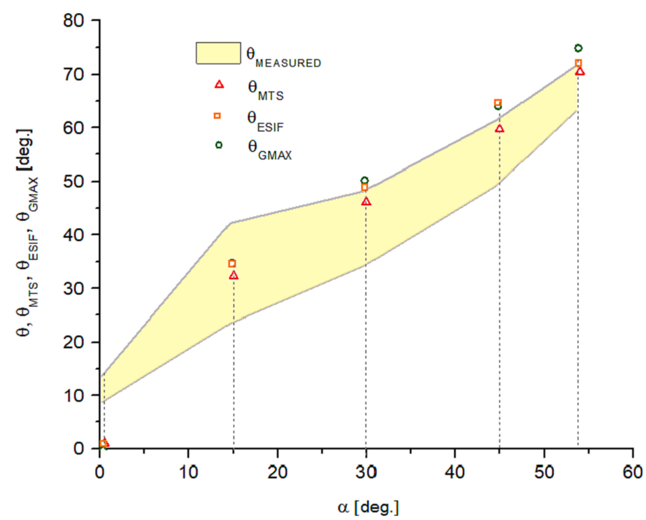

Fig. 12. Measured and theoretical crack initiation angles (θ, θ_{MTS}, θ_{ESIF}, θ_{Gmax}) according to crack orientation (α).

$$G(\theta) = \frac{4}{E'}\left(\frac{1}{3 + cos^2(\theta)}\right)^2\left(\frac{1 - \frac{\theta}{\pi}}{1 + \frac{\theta}{\pi}}\right)^{\frac{\theta}{\pi}}\left[\left(1 + 3cos^2(\theta)\right)K_I^2 + 8sin(\theta)cos(\theta)K_I K_{II} + \left(9 - 5cos^2(\theta)\right)K_{II}^2\right] \tag{6}$$

$$\left(\frac{1}{3 + cos^2(\theta_c)}\right)^2\left(\frac{1 - \frac{\theta_c}{\pi}}{1 + \frac{\theta_c}{\pi}}\right)^{\frac{\theta_c}{\pi}}\left[\left(1 + 3cos^2(\theta_c)\right)\left(\frac{K_I}{K_{Ic}}\right)^2 + 8sin(\theta_c)cos(\theta_c)\left(\frac{K_I K_{II}}{K_{Ic}^2}\right) + \left(9 - 5cos^2(\theta_c)\right)\left(\frac{K_{II}}{K_{Ic}}\right)^2\right] = 1 \tag{7}$$

Table 4
Predicted and experimental fracture test results for the SLS-PA2200 printed specimens.

α [°]	K_I/K_{IC}				K_{II}/K_{IC}				Crack initiation angles			
	Exp.	MTS	Gmax	ESIF	Exp.	MTS	Gmax	ESIF	$\theta_{Exp.}$ [°]	θ_{MTS} [°]	θ_{Gmax} [°]	θ_{ESIF} [°]
0	1.00 (0.22)	1.00	1.00	1.00	0.00 (0.00)	0.00	0.00	0.00	11.28 (2.46)	0.00	0.00	0.00
15	0.82 (0.18)	0.90	0.90	0.90	0.28 (0.06)	0.24	0.23	0.10	32.96 (9.36)	32.28	34.92	34.56
30	0.48 (0.05)	0.72	0.72	0.78	0.31 (0.03)	0.43	0.39	0.15	35.25 (5.03)	46.16	49.99	48.94
45	0.25 (0.05)	0.53	0.53	0.61	0.43 (0.08)	0.57	0.49	0.20	55.39 (6.09)	59.70	64.35	64.72
54	0.00 (0.00)	0.40	0.40	0.52	0.33 (0.02)	0.65	0.54	0.23	67.54 (4.25)	70.52	75.23	72.10

3.2.3. Equivalent stress intensity factor (ESIF) criterion

A generalized fracture criterion based on the equivalent stress intensity factor K_{eq}, which is defined similar to maximum principal stress and expressed as in the eq. (8) [68,69].

$$K_{eq} = \frac{K_I}{2} + \frac{1}{2}\sqrt{K_I^2 + 4(\lambda \bullet K_{II})^2} \leq K_{Ic} \tag{8}$$

with $\lambda = K_{Ic}/K_{IIc}$. Crack starts to propagate when K_{eq} reaches the fracture toughness of the material K_{Ic}. The initiation angle can be computed using eq. (9).

$$\theta_c = \mp\left(155.5^0 \frac{|K_{II}|}{|K_I| + |K_{II}|}\right) - 83.4^0\left(\frac{|K_{II}|}{|K_I| + |K_{II}|}\right)^2 \tag{9}$$

Fig. 11 shows the experimental results and the fracture limit curves predicted by the MTS, Gmax and ESIF criteria. Comparing the obtained data with the considered fracture criteria, it can be observed that all experimental results are largely included between the three criteria. However, the limit curves of Gmax and ESIF criteria show the best match with the experimental data. Thus, the obtained results are bordered to the upper limit by the Gmax criterion and to the lower limit by the ESIF criterion. Nevertheless, it can be easily seen that, regardless of the crack angle, the fracture toughness results show a large spread.

The experimental (θ) and predicted (θ_{MTS}, θ_{ESIF}, θ_{Gmax}) crack initiation angles depending on the crack angle (α) are shown in Fig. 12. The obtained results are in good agreement with the classical fracture theories of the crack initiation angles. However, by comparing three different failure criteria, including MTS, Gmax and ESIF, in various α ranges from mode I (α = 0°) to mode II (α = 54°), MTS predictions can be considered the most acceptable, highlighting the smallest errors in respect of the experimental results. Reasonable results are also obtained in the case of the ESIF criterion. This representation suggests that classical fracture criteria could be successfully applied to laser-sintered manufactured specimens.

Even so the initiation angle is rather an angular interval than a single value for each crack angle, the theoretical angular predictions tend to overestimate the real values. The angular interval of initiation angle defines the highest instability for 15° crack. This specific angle seems to be a weak spot, where interlayer and intralayer fracture are alternating without a decisive fracture preference. The discrete values of predicted and experimental fracture test results are presented in the Table 4.

4. Conclusions

The paper presents theoretical and experimental data on mixed-mode I/II fracture properties of laser sintered polyamide. The experiment was conducted on SCB specimens manufactured from polyamide PA2200 having 0, 15, 30, 45 and 54° crack orientation angles. In this way, the full range starting from pure mode I to pure mode II fracture properties are covered. The following conclusions can be drawn from the investigations:

- The investigated PA2200 specimens have a mode I fracture toughness (K_{IC}) of 1.25 MPa·m$^{0.5}$ and mode II fracture toughness (K_{IIC}) of 0.37 MPa·m$^{0.5}$, respectively. Between the two pure modes of fracture (I and II), three other mixed modes were obtained.
- Contrary to the fracture toughness values, the fracture energy in mode I loading is about 60.5 % lower than that obtained in mode I.
- The tested SCB specimens showed plastic indentation, both in the area of the support pins and under the loading pin, predominantly in the pure mode II loading.
- The layered and orthotropic nature of the SLS manufacturing process dictates the crack trajectory in SCB specimens. It was found that, the crack propagates along the weaker plane, following an interlayer-to-intralayer fracture transition (like zig-zag pattern).
- The fracture toughness and crack initiation angles were compared with three fracture criteria (Maximum Tensile Stress-MTS, Maximum Energy Release Rate-Gmax and Equivalent Stress Intensity Factor-ESIF). It was obtained that Gmax and ESIF theoretical criteria present the best prediction of the experimental results.

CRediT authorship contribution statement

Dan Ioan Stoia: Conceptualization, Formal analysis, Investigation, Writing – original draft, Writing – review & editing. **Emanoil Linul:** Conceptualization, Investigation, Writing – original draft, Writing – review & editing. **Liviu Marsavina:** Conceptualization, Resources, Writing – original draft, Writing – review & editing, Funding acquisition.

Declaration of Competing Interest

The authors declare that they have no known competing financial interests or personal relationships that could have appeared to influence the work reported in this paper.

Data availability statement

The data that support the findings of this study are available from the corresponding author, [Emanoil Linul], upon reasonable request.

Acknowledgement

This research was partially funded by research grant from the European Union's Horizon 2020 research and innovation program under grant agreement No 857124.

References

[1] M.R. Khosravani, P. Soltani, T. Reinicke, Fracture and structural performance of adhesively bonded 3D-printed PETG single lap joints under different printing parameters, Theor. Appl. Fract. Mech. 116 (2021), 103087.

[2] M. Lorenzo-Bañuelos, A. Díaz, I.I. Cuesta, Influence of raster orientation on the determination of fracture properties of polypropylene thin components produced by additive manufacturing, Theor. Appl. Fract. Mech. 107 (2020), 102536.

[3] S. Cicero, V. Martínez-Mata, L. Castanon-Jano, et al., Analysis of notch effect in the fracture behaviour of additively manufactured PLA and graphene reinforced PLA, Theor. Appl. Fract. Mech. 114 (2021), 103032.

[4] S. Shahbaz, M.R. Ayatollahi, M. Petru, A.R. Torabi, U-notch fracture in additively manufactured ABS specimens under symmetric three-point bending, Theor. Appl. Fract. Mech. 119 (2022), 103318.
[5] L. Lanzl, K. Wudy, D. Drummer, The effect of short glass fibers on the process behavior of polyamide 12 during selective laser beam melting, Polym. Test. 83 (2020), 106313.
[6] S. Yuan, X. Yu, Ultrasonic non-destructive evaluation of selectively laser-sintered polymeric nanocomposites, Polym. Test. 90 (2020), 106705.
[7] D.I. Stoia, L. Marsavina, E. Linul, Mode I fracture toughness of polyamide and alumide samples obtained by selective laser sintering additive process, Polymers 12 (3) (2020) 640.
[8] T. Puttonen, M. Salmi, J. Partanen, Mechanical properties and fracture characterization of additive manufacturing polyamide 12 after accelerated weathering, Polym. Test. 104 (2021), 107376.
[9] L.J. Tan, W. Zhu, K. Sagar, K. Zhou, Comparative study on the selective laser sintering of polypropylene homopolymer and copolymer: processability, crystallization kinetics, crystal phases and mechanical properties, Addit Manuf. 37 (2020), 101610.
[10] D. Xie, R. Dittmeyer, Correlations of laser scanning parameters and porous structure properties of permeable materials made by laser-beam powder-bed fusion, Addit Manuf. 47 (2021), 102261.
[11] S. Petzold, J. Klett, A. Schauer, A. Osswald, Surface roughness of polyamide 12 parts manufactured using selective laser sintering, Polym. Test. 80 (2019), 106094.
[12] M. Moussaoui, S. Amroune, A. Tahiri, B.K. Hachi, Brittle fracture investigation from disc specimen weakened by U- notch in mixed mode I + II, Eng. Fract. Mech. 8 (2020) 337–352.
[13] M.R.M. Aliha, M.R. Ayatollahi, Geometry effects on fracture behaviour of polymethyl methacrylate, Mater. Sci. Eng. A 527 (3) (2010) 526–530.
[14] M.R.M. Aliha, S.S. Mousavi, S.M.N. Ghoreishi, Fracture load prediction under mixed mode I+II using a stress based method for brittle materials tested with the asymmetric four-point bend specimen, Theor. Appl. Fract. Mech. 103 (2019), 102249.
[15] M.R.M. Aliha, H.G. Kucheki, M. Mirsayar, Mixed Mode I/II Fracture Analysis of Bi-Material Adhesive Bonded Joints Using a Novel Short Beam Specimen, Appl. Sci. 11 (11) (2021) 5232.
[16] S.A. Saed, H.R. Karimi, S.M. Rad, M.R.M. Aliha, X. Shi, P.J. Haghighatpour, Full range I/II fracture behavior of asphalt mixtures containing RAP and rejuvenating agent using two different 3-point bend type configurations, Constr. Build. Mater. 314 (2022) 125590.
[17] M.R.M. Aliha, S.S. Mousavi, Sub-sized short bend beam configuration for the study of mixed-mode fracture, Eng. Fract. Mech. 225 (2020), 106830.
[18] M.R.M. Aliha, S.S. Samareh-Mousavi, M.M. Mirsayar, Loading rate effect on mixed mode I/II brittle fracture behavior of PMMA using inclined cracked SBB specimen, Int. J. Solids Struct. 232 (2021), 111177.
[19] S.S. Mousavi, M.R.M. Aliha, D.M. Imani, On the use of edge cracked short bend beam specimen for PMMA fracture toughness testing under mixed-mode I/II, Polym Test. 81 (2019), 106199.
[20] M.R.M. Aliha, S. Bagherifard, S.h. Akhondi, S.S. Mousavi, A. Mousavi, H. Parsania, Fracture and microstructural study of bovine bone under mixed mode I/II loading, Procedia Structural Integrity 13 (2018) 1488–1493.
[21] M.R.M. Aliha, H.R. Karimi, S.M.N. Ghoreishi, Design and validation of simple bend beam specimen for covering the full range of I+II fracture modes, Eur. J. Mech. A/Solids 91 (2022), 104425.
[22] M.R.M. Aliha, P.J. Haghighatpour, A. Tavana, Application of asymmetric semi-circular bend test for determining mixed mode I + II fracture toughness of compacted soil material, Eng. Fract. Mech. 262 (2022), 108268.
[23] M.R.M. Aliha, S.S. Mousavi, A. Bahmani, E. Linul, L. Marsavina, Crack initiation angles and propagation paths in polyurethane foams under mixed modes I/II and I/III loading, Theor. Appl. Fract. Mech. 101 (2019) 152–161.
[24] D.M. Imani, M.R.M. Aliha, E. Linul, L. Marsavina, A suitable mixed mode I/II test specimen for fracture toughness study of polyurethane foam with different cell densities, Theor. Appl. Fract. Mech. 117 (2022), 103171.
[25] L. Marsavina, D.M. Constantinescu, E. Linul, F.A. Stuparu, D.A. Apostol, Experimental and numerical crack paths in PUR foams, Eng. Fract. Mech. 167 (2016) 68–83.
[26] M.R.M. Aliha, F. Berto, A. Bahmani, P. Gallo, Mixed mode I/II fracture investigation of Perspex based on the averaged strain energy density criterion, Phys. Mesomech. 20 (2) (2017) 149–156.
[27] M.R.M. Aliha, F. Berto, A. Mousavi, S.M.J. Razavi, On the applicability of ASED criterion for predicting mixed mode I+II fracture toughness results of a rock material, Theor. Appl. Fract. Mech. 92 (2017) 198–204.
[28] M.R. Ayatollahi, M.R.M. Aliha, Analysis of a new specimen for mixed mode fracture tests on brittle materials, Eng. Fract. Mech. 76 (11) (2009) 1563–1573.
[29] A. Bahmani, M.R.M. Aliha, M.J. Sarbijan, S.S. Mousavi, An extended edge-notched disc bend (ENDB) specimen for mixed-mode I+II fracture assessments, Int. J. Solids Struct. 193–194 (2020) 239–250.
[30] A. Mousavi, M.R.M. Aliha, D.M. Imani, Effects of biocompatible Nanofillers on mixed-mode I and II fracture toughness of PMMA base dentures, J. Mech. Behav. Biomed. Mater. 103 (2019), 103566.
[31] S.M.J. Razavi, M.R.M. Aliha, F. Berto, Application of an average strain energy density criterion to obtain the mixed mode fracture load of granite rock tested with the cracked asymmetric four-point bend specimens, Theor. Appl. Fract. Mech. 97 (2018) 419–425.
[32] M.R. Ayatollahi, M.R.M. Aliha, M.M. Hassani, Mixed mode brittle fracture in PMMA-An experimental study using SCB specimens, Mater. Sci. Eng. A. 417 (1–2) (2006) 348–356.
[33] M.R.M. Aliha, M.R. Ayatollahi, Mixed mode I/II brittle fracture evaluation of marble using SCB specimen, Proc. Eng. 10 (2011) 311–318.
[34] L. Marsavina, D.M. Constantinescu, E. Linul, D.A. Apostol, T. Voiconi, T. Sadowski, Refinements on fracture toughness of PUR foams, Eng. Fract. Mech. 129 (2014) 54–66.
[35] B. Ameri, F. Taheri-Behrooz, M.R.M. Aliha, Evaluation of the geometrical discontinuity effect on mixed-mode I/II fracture load of FDM 3D-printed parts, Theor. Appl. Fract. Mech. 113 (2021), 102953.
[36] B. Bahrami, M.R. Ayatollahi, I. Sedighi, M.A. Pérez, A.A. Garcia-Granada, The effect of in-plane layer orientation on mixed-mode I-II fracture behavior of 3D-printed poly-carbonate specimens, Eng. Fract. Mech. 231 (2020) 107018.
[37] M.R. Khosravani, F. Berto, M.R. Ayatollahi, T. Reinicke, Fracture behavior of additively manufactured components: A review, Theor. Appl. Fract. Mech. 109 (2020) 102763.
[38] A.M. Oviedo, A.H. Puente, C. Bernal, E. Pérez, Mechanical evaluation of polymeric filaments and their corresponding 3D printed samples, Polym. Test. 88 (2020) 106561.
[39] J. Fonseca, I.A. Ferreira, M.F.S.F. de Moura, M. Machado, J.L. Alves, Study of the interlaminar fracture under mode I loading on FFF printed parts, Comput. Struct. 214 (2019) 316–324.
[40] C. Vălean, L. Marșavina, M. Mărghitaș, E. Linul, J. Razavi, F. Berto, R. Brighenti, The effect of crack insertion for FDM printed PLA materials on Mode I and Mode II fracture toughness, Procedia Structural Integrity 28 (2020) 1134–1139.
[41] L. Marșavina, C. Vălean, M. Mărghitaș, et al., Effect of the manufacturing parameters on the tensile and fracture properties of FDM 3D-printed PLA specimens, Eng. Fract. Mech. (2022) paper accepted.
[42] C. Vălean, L. Marșavina, M. Mărghitaș, E. Linul, J. Razavi, F. Berto, Effect of manufacturing parameters on tensile properties of FDM printed specimens, Procedia Structural Integrity 26 (2020) 313–320.
[43] B. Ameri, F. Taheri-Behrooz, M.R.M. Aliha, Fracture Loads Prediction of the Modified 3D-Printed ABS Specimens Under Mixed-Mode I / II Loading, Eng. Fract. Mech. 235 (2020), 107181.
[44] B. Ameri, F. Taheri-Behrooz, M.R.M. Aliha, Mixed-mode tensile/shear fracture of the additively manufactured components under dynamic and static loads, Eng. Fract. Mech. 260 (2022), 108185.
[45] T.M. Brugo, I. Campione, G. Minak, Investigation by Digital Image Correlation of mixed-mode I and II fracture behavior of polymeric IASCB specimens with additive manufactured crack-like notch, Materials 14 (2021) 1084.
[46] I. Campione, T.M. Brugo, G. Minak, et al., Investigation by Digital Image Correlation of mixed mode I and II fracture behavior of metallic IASCB specimens with additive manufactured crack-like notch, Metals 10 (2020) 400.
[47] Y. Liu, S. Mahadevan, Threshold stress intensity factor and crack growth rate prediction under mixed-mode loading, Eng. Fract. Mech. 74 (3) (2007) 332–345.
[48] E. Linul, L. Marșavina, D.I. Stoia, Mode I and II fracture toughness investigation of Laser-Sintered Polyamide, Theor. Appl. Fract. Mech. 106 (2020), 102497.
[49] D.I. Stoia, L. Marsavina, E. Linul, Mode I critical energy release rate of additively manufactured polyamide samples, Theor. Appl. Fract. Mech. 114 (2021), 102968.
[50] ASTM D5045-14, Standard Test Methods for Plane-Strain Fracture Toughness and Strain Energy Release Rate of Plastic Materials, 2014.
[51] E. Linul, L. Marșavina, C. Vălean, R. Bănică, Static and dynamic mode I fracture toughness of rigid PUR foams under room and cryogenic temperatures, Eng. Fract. Mech. 225 (2020), 106274.
[52] E. Linul, L. Marsavina, Prediction of fracture toughness for open cell polyurethane foams by finite-element micromechanical analysis, Iran. Polym. J. 20 (9) (2011) 735–746.
[53] L. Marsavina, E. Linul, Fracture toughness of rigid polymeric foams: A review, Fatig. Fract. Eng. Mater. Struct. 43 (11) (2020) 2483–2514.
[54] M.R. Ayatollahi, M.R.M. Aliha, Wide range data for crack tip parameters in two disc-type specimens under mixed mode loading, Comput. Mater. Sci. 38 (4) (2007) 660–670.
[55] A.S. Fayed, Numerical evaluation of mode I/II SIF of quasi-brittle materials using cracked semi-circular bend specimen, Eng. Solid Mech. 6 (2) (2018) 175–186.
[56] D.I. Stoia, E. Linul, L. Marsavina, Influence of manufacturing parameters on mechanical properties of porous materials by Selective Laser Sintering, Materials 12 (6) (2019) 871.
[57] D.I. Stoia, L. Marsavina, E. Linul, Correlations between process parameters and outcome properties of Laser-Sintered polyamide, Polymers 11 (11) (2019) 1850.
[58] M.R.M. Aliha, M.R. Ayatollahi, D.J. Smith, M.J. Pavier, Geometry and size effects on fracture trajectory in a limestone rock under mixed mode loading, Eng. Fract. Mech. 77 (11) (2010) 2200–2212.
[59] M.R.M. Aliha, A. Bahmani, S.h. Akhondi, Mixed mode fracture toughness testing of PMMA with different three-point bend type specimens, Eur. J. Mech. A/Solids 58 (2016) 148–162.
[60] M.R.M. Aliha, M.R. Ayatollahi, J. Akbardoost, Typical Upper Bound-Lower Bound Mixed Mode Fracture Resistance Envelopes for Rock Material, Rock Mech. Rock Eng. 45 (1) (2012) 65–74.
[61] A. Nabavi-Kivi, M.R. Ayatollahi, P. Rezaeian, S.M.J. Razavi, Investigating the effect of printing speed and mode mixity on the fracture behavior of FDM-ABS specimens, Theor. Appl. Fract. Mech. 118 (2022), 103223.
[62] L. Marsavina, D.I. Stoia, E. Linul, Mixed modes crack paths in SCB specimens obtained via SLS, Procedia Struct. Integrity 39 (2022) 801–807.
[63] H.R. Fattahi Amirdehi, M.R.M. Aliha, A. Moniri, A.R. Torabi, Using the generalized maximum tangential stress criterion to predict mode II fracture of hot mix asphalt in terms of mode I results – A statistical analysis, Constr. Build. Mater. 213 (2019) 483–491.

[64] M.M. Mirsayar, F. Berto, M.R.M. Aliha, P. Park, Strain-based criteria for mixed-mode fracture of polycrystalline graphite, Eng. Fract. Mech. 156 (2016) 114–123.
[65] M.M. Mirsayar, A. Razmi, M.R.M. Aliha, F. Berto, EMTSN criterion for evaluating mixed mode I/II crack propagation in rock materials, Eng. Fract. Mech. 190 (2018) 186–197.
[66] F. Erdogan, G.C. Sih, On the crack extension in plates under plane loading and transverse shear, J. Basic Eng. ASME 85 (1963) 519–527.
[67] M.A. Hussain, S.L. Pu, J. Underwood, Strain energy release rate for a crack under combined Mode I and II, Fracture Analysis, ASTM STP 560 (1974) 2–28.
[68] H.A. Richard, Bruchvorhersagen bei uberlagreter normal- und schubbeanspruchung von rissen, VDI-Verlag, 1985.
[69] H.A. Richard, M. Fulland, M. Sander, Theoretical crack path prediction, Fatig. Fract. Eng, Mater. Struct. 28 (1-2) (2005) 3–12.